HOKKAIDO UNIVERSITY

Title	Effect of introducing somatic mitochondria into an early embryo on zygotic gene activation
Author(s)	Hayashi, Yoshihiro; Bai, Hanako; Takahashi, Masashi et al.
Citation	Biology of reproduction, 112(4), 614-627 https://doi.org/10.1093/biolre/ioaf010
Issue Date	2025-01-15
Doc URL	https://hdl.handle.net/2115/97411
Rights	This is a pre-copyedited, author-produced version of an article accepted for publication in Biology of reproduction following peer review. The version of record Biology of Reproduction, Volume 112, Issue 4, April 2025, Pages 614-627, is available online at: https://doi.org/10.1093/biolre/ioaf010.
Type	journal article
File Information	BOR_hayashi.pdf

Hokkaido University Collection of Scholarly and Academic Papers : HUSCAP

Title

Effect of introducing somatic mitochondria into an early embryo on zygotic gene activation

Authors

Yoshihiro Hayashi[a], Hanako Bai[a], Masashi Takahashi[b], Tomohiro Mitani[c], and Manabu Kawahara[a]*

[a] Laboratory of Animal Genetics and Reproduction, Research Faculty of Agriculture, Hokkaido University, Sapporo, 060-8589, Japan, [b] Global Station for Food, Land and Water Resources, Global Institution for Collaborative Research and Education, Hokkaido University, Sapporo, Hokkaido 060-8589, Japan, [c] Laboratory of Animal Production System, Research Faculty of Agriculture, Hokkaido University, Sapporo, Japan.

***Correspondence**: Dr. Manabu Kawahara, PhD

Laboratory of Animal Genetics and Reproduction, Graduate School of Agriculture,

Hokkaido University, Sapporo 060-8589, Japan

Tel. & Fax: +81 11 706 2541

E-mail address: k-hara@agr.hokudai.ac.jp

Grant support

This work was supported by the Japan Society for the Promotion of Science (JSPS), KAKENHI Grant Number 24K01902.

Running title.

Relationship between mitochondria and ZGA

Summary Sentence

Mismatch between cell differentiation and mitochondrial maturity prevents transition from minor to major ZGA in mouse embryos.

Keywords

Histone modifications; Mitochondria; Mitochondrial remodeling; Preimplantation mouse embryo; Zygotic gene activation.

Abstract

Unlike differentiated somatic cells, which possess elongated mitochondria, undifferentiated cells, such as those of preimplantation embryos, possess round, immature mitochondria. Mitochondrial morphology changes dynamically during cell differentiation in a process called mitochondrial maturation. The significance of the alignment between cell differentiation and mitochondrial maturity in preimplantation development remains unclear. In this study, we analyzed mouse embryos into which liver-derived somatic mitochondria were introduced (SM-embryos). Most SM-embryos were arrested at the two-cell stage. Some of the introduced somatic mitochondria became round, while others remained elongated and large. RNA-sequencing revealed a disruption of both minor and major zygotic gene activation (ZGA) in SM-embryos. Minor ZGA did not terminate before major ZGA, and the onset of major ZGA was inhibited, as shown by histone modification analyses of histone H3 lysine 4 trimethylation and histone H3 lysine 27 acetylation. Further analysis of metabolites involved in histone modification regulation in SM-embryos showed a significantly lower NAD^+/NADH ratio in SM-embryos than in control embryos. Additionally, the mitochondrial membrane potential, an indicator of mitochondrial function, was lower in SM-embryos than in control embryos. Our results demonstrated that introducing somatic mitochondria into an embryo induces mitochondrial dysfunction, thereby disrupting metabolite production, leading to a disruption in ZGA and inducing developmental arrest. Our findings reveal that the alignment between cell differentiation and mitochondrial maturity is essential for early embryonic development.

Introduction

Mitochondria are involved in a wide range of cellular physiological activities, including

adenosine triphosphate (ATP) synthesis, reactive oxygen species (ROS) production, calcium ion homeostasis, cellular signaling pathway activities, cell death induction, and cellular metabolite synthesis [1–4]. Hence, all eukaryotic cells inevitably possess mitochondria to ensure their survival. However, mitochondrial morphology and activity differ between differentiated somatic cells and undifferentiated early embryos. Mitochondrial morphology changes dynamically during cell differentiation, particularly during oogenesis and early embryogenesis [5,6].

Oocyte mitochondria undergo significant ultrastructural changes during early embryogenesis. In human ovaries, primordial germ cells (PGCs) mitochondria are spherical, with a clear matrix and small vesicular cristae [7]. Human oocyte and zygote mitochondria are also spherical in shape, and possess a dense matrix and peripheral arched cristae [7,8]. During the 2- to 8-cell cleavage stages of embryonic development, most mitochondria remain spherical; however, some exhibit an elongated morphology (with height approximately three times the width) [7]. As cell differentiation progresses, mitochondria elongate, and cristae develop. These mitochondrial morphological changes have been observed during early embryogenesis in mice [9,10] and cattle [11], suggesting that such changes are unique to mammalian embryos. In mouse [12] and bovine [13] blastocysts, as compared to undifferentiated inner cell mass (ICM) mitochondria, trophectoderm (TE) mitochondria are elongated.

Mitochondrial morphology is involved in the regulation of metabolism [14], as mitochondrial membranes and cristae structures are sites of energy synthesis-related processes, including oxidative phosphorylation (OXPHOS) [14,15]. Mitochondrial elongation leads to increased OXPHOS activity and enhances ATP production [16]. Structural changes in cristae associated with mitochondrial elongation are also

necessary for increased OXPHOS activity [17]. In addition, in blastocyst-stage embryos, OXPHOS activity is higher in TE cells with elongated mitochondria than in ICM cells with spherical mitochondria [18]. These findings suggest that mitochondrial morphology and function during early embryogenesis are related to cell differentiation regulation.

Mitochondrial morphological and functional alterations, mitochondrial maturation, are important for cell differentiation during early embryogenesis[19–21]. However, the significance of the alignment between the cell differentiation state and mitochondrial maturity has not yet been elucidated. Embryonic metabolism changes during embryonic development [22]. Recently, it was reported that the nuclear localization of mitochondrial tricarboxylic acid (TCA) cycle enzymes is related to zygotic gene activation (ZGA) [23]. However, the relationship between ZGA and metabolites synthesized in the immature mitochondria of early embryos has not yet been investigated in detail. In this study, we evaluated the relationship between cell differentiation and mitochondrial maturity by introducing mature mitochondria, derived from differentiated somatic cells, into zygotes with immature mitochondria. We aimed to elucidate a new aspect of mitochondrial function during early embryogenesis by analyzing embryos into which somatic mitochondria were introduced. Specifically, we investigated the transcriptional regulation of ZGA, a nuclear reprogramming event that transitions the genome from a state of transcriptional quiescence to robust transcriptional activity.

Materials and methods

Ethical approval

All research protocols were approved by the Regulatory Committee for the Care and Use of Laboratory Animals of Hokkaido University.

Preparation of mouse embryos

Mouse embryos were prepared by *in vitro* fertilization following a previously described procedure[24]. Oocyte and liver donors were ICR female mice.

Microinjection of somatic mitochondria into zygotes

Mitochondrial isolation and microinjection into zygotes were performed following previously described methods, with slight modifications [25,26]. Three livers were harvested from female ICR mice and resuspended in an isolation buffer (210 mM mannitol, 70 mM sucrose, 5 mM HEPES, 1 mM KCl, and 1 mM EGTA, pH 7.2, containing 0.5% bovine serum albumin [BSA] Sigma, St. Louis, MO, USA). The homogenate was centrifuged twice at 800 × *g* for 10 min at 4°C. Then, the supernatant was decanted and centrifuged at 10,000 × *g* for 20 min at 4°C. The resulting mitochondrial pellet was resuspended in a respiration buffer (225 mM mannitol, 75 mM sucrose, 10 mM KCl, 10 mM Tris-HCl, and 5 mM KH_2PO_4, pH 7.2). The isolated mitochondria were then maintained at 4°C until the time of microinjection as previously described [27,28]. The mitochondrial suspensions were placed on a working plate, and settled mitochondria were picked using a glass pipette. Approximately 2 picolitres (pL) of the mitochondrial suspension were injected into the zygotes at 6–9 hours post-insemination (hpi) using a Piezo micromanipulator (Prime-Tech, Tokyo, Japan) in M2 medium. After preparation of the mitochondrial suspension, each microinjection process was performed in less than one hour per trial. Similarly, microinjection of buffer

for experimental control was carried out at 6–9 hpi.

Library preparation for RNA-seq

Total RNA from two-cell embryos (intact: 32–33 hpi; SM: 35–36 hpi) was extracted using the ReliaPrep RNA Cell Miniprep System (Promega, Madison, WI, USA). Twenty embryos per sample were used for each replicate. cDNA was synthesized and amplified using the SMART-Seq V4 Ultra Low Input RNA Kit for Sequencing 480 Rxns (Takara Bio, Shiga, Japan). Libraries were constructed using the NEBNext Ultra II RNA Library Prep Kit (New England Biolabs Inc, Ipswich, Massachusetts, USA). RNA concentration and fragment distribution were assessed using the Qubit (Thermo Fisher Scientific, Waltham, MA, USA) and AATI-Fragment Analyzer (Illumina, San Diego, CA, USA), respectively. Sequencing was performed based on a 150-bp paired-end format using the NovaSeq 6000 (Illumina).

RNA-seq data analysis

Sequencing reads were mapped to the *Mus musculus* genome assembly (GRCm39/mm39) using the hisat2 software. Fragments per kilobase of exon per million mapped reads (FPKM) values were calculated for each gene and used in subsequent analyses. Genes with FPKM ≥1 were considered as expressed. Differential gene expression (DEG) analysis was performed using the DESeq2 (https://bioconductor.org/packages/release/bioc/html/DESeq2.html) for biological replicates and the edgeR (https://bioconductor.org/packages/release/bioc/html/edgeR.html) for non-biological replicates, by normalizing the expression values. Genes with |log2(FoldChange)| ≥ 1

and Padj ≤ 0.05 were considered as DEGs (Table S1). Hierarchical clustering analyses were performed using the R package (https://www.r-project.org/). All DEGs were screened for major (Table S2) and minor ZGA-related genes (Table S3) using the DBTMEE (http://dbtmee.hgc.jp/).

Quantitative PCR (qPCR)

Total RNA extraction, cDNA synthesis, and subsequent analyses were performed as previously described [29]. Total RNA from one-cell-stage embryos (10 hpi) and late two-cell-stage embryos (Intact: 32–33 hpi, SM: 35–36 hpi) was extracted using the ReliaPrep RNA Cell Miniprep System (Promega). cDNA synthesis was performed using the ReverTra Ace qPCR RT Master Mix (Toyobo, Osaka, Japan). qPCR was performed after preparing the reaction mixtures using the THUNDERBIRD SYBR qPCR Mix (Toyobo). The primer sets used for qPCR analysis are listed in Table S4. The thermal cycling conditions were: 1 cycle at 95°C for 30 s, followed by 45 cycles at 95°C for 15 s, 55°C for 30 s, and 72°C for 30 s. The relative abundance of mRNA was calculated based on the expression levels of *Gapdh*. Ten independent embryo samples were used for each experiment, and the results are presented as the means of seven to eight biological replicates per group in a single qPCR run.

Antibody staining for immunofluorescence

The zona pellucida of embryos was removed using acidic Tyrode's solution for 30 seconds [30]. For immunofluorescence staining, embryos lacking the zona pellucida were fixed with 4% paraformaldehyde (PFA) in phosphate-buffered saline (PBS) for 30 min and then permeabilized with 0.4% Triton X-100 in PBS for 30 min. Subsequently,

the embryos were blocked for 30 min with blocking solution (Table S5). Primary antibodies were diluted in Can Get Signal® immunostain Immunoreaction Enhancer Solution A (NKB-501, Toyobo); the primary antibody dilutions are listed in Table S5. The primary antibody reaction occurred overnight at 4°C. The secondary antibody, Alexa Fluor 555 goat anti-rabbit IgG (A21428, polyclonal, 1:400; Thermo Fisher Scientific), was diluted in PBS containing 1% BSA and 0.1% Triton-100. The secondary antibody reaction was performed as indicated in Table S5. Nuclei were counterstained with 25 µg/mL Hoechst 33342 (Sigma) for 10 min at 25°C. Fluorescence signals were visualized using a TCS SP5 confocal laser scanning microscope (Leica, Wetzlar, Germany).

Electron microscopy

Electron microscopy of embryos was performed as previously described [13]. The embryos were fixed in 2.5% glutaraldehyde (TAAB Laboratories, Reading, UK) in a 0.1 M phosphate buffer (pH 7.2) for 2 h at 4°C. After post-fixation in 1% osmium tetroxide (Nisshin EM, Tokyo, Japan) for 2 h at 4°C, the specimens were dehydrated in a graded series of ethanol. After ethanol removal using propylene oxide, the specimens were embedded in epoxy resin 812 (TAAB Laboratories). Semi-thin sections (500 nm) were cut for light microscopic examination and stained with toluidine blue for further sectioning. Ultrathin sections (80 nm) were prepared using an ultramicrotome (ULTRACUTN, Reichert-Nissei, Buffalo, NY, USA), collected on copper grids, post-stained with 2% uranyl acetate (MERCK, Darmstadt, Germany) and lead citrate, and examined using a Transmission electron microscopy (TEM) (JEM-2100, JEOL Tokyo, Japan).

Immunogold electron microscopy

Immunogold electron microscopy was performed as previously described [31]. Fixation and embedding were performed as for electron microscopy. Nickel grids carrying ultrathin sections (80 nm) were incubated in 0.5 M Nametaperiodate ($NaIO_4$) for 30 min to remove excess fixatives. After washing in distilled H_2O, the grids were transferred to a 0.1 N HCl solution for 10 min to remove excess osmium tetroxide. Then, the grids were briefly washed and blocked in 0.1 M glycine in PBS for 30 min to inactivate residual aldehydes. After washing with PBS, the sections were blocked with a second blocking buffer (PBS containing 1% BSA) for 45 min. Next, the grids were incubated in the primary mouse anti-cytochrome C antibodies (Abcam, Cambridge, UK) diluted at a 1:10 ratio in the second blocking buffer at 4°C, for 3 days. Then, the grids were washed in PBS and incubated with goat anti-mouse IgG in 10 nm gold (EMGMHL10, polyclonal, 1:20; BBI Solutions, Portland, MN, USA) at room temperature for 2 hours. After three washes in PBS for 5 min and two washes in distilled H_2O for 5 min, the grids were post-stained and examined as described Electron microscopy.

Measurement of NAD+ and NADH levels

NAD^+ and NADH levels were determined using the NAD^+/NADH Glo cycling assay, according to the instructions of the manufacturer (Promega, Madison, WI, USA). Briefly, 20 embryos at 27–28 hpi were lysed with a carbonate-buffered base solution containing 1% DTAB (Sigma), 10 mM nicotinamide (Wako), and 0.05% Triton X-100, pH 10.7, and incubated for 10 min at room temperature. The sample solution was frozen in liquid nitrogen and stored at -80°C until the time of the experiment. Upon

thawing, the sample solution was divided into two tubes (25 μL per tube). For NAD^+ measurement, 12.5 μL of 0.4 N HCl was added to the solution, which was heated at 60 °C for 15 min. After cooling for 10 min through incubation at room temperature, 12.5 μL of 0.5 M Trizma base (Sigma) was added to the resulting samples. The sample solution was heated at 60 °C for 15 min for NADH measurement. After 10 min of incubation at room temperature, 12.5 μL of 0.5 M Trizma base and 12.5 μL of 0.4 N HCl were added to the sample solution. Next, the assay reagent was added to the sample solution and incubated for 3 h before cycling. Fluorescence intensity was measured using a multimode plate reader (ARVO X4; PerkinElmer, Waltham, MA, USA). To establish the standard curve, we used 0, 0.5, 1, 10, and 50 nmol/L β-NAD (Sigma) in PBS.

Measurement of ROS levels

Embryos were treated with 5 μM CellROX™ Green Reagent (Invitrogen) in M2 medium to evaluate intracellular ROS levels. After incubation, all embryos were stained in the dark at 37°C for 30 min and subsequently washed thrice with M2 medium. Treated embryos were fixed with 4% PFA in PBS for 30 min. Fluorescence signals were detected using a DMi8 fluorescence microscope (Leica), and fluorescence intensities were analyzed using the ImageJ software (National Institutes of Health, https://imagej.nih.gov/ij/index.html). ROS levels were determined using collecting approximately five embryos collected at a time, with each experiment conducted in triplicate.

Measurement of mitochondrial membrane potential through JC-10 staining

To evaluate the mitochondrial membrane potential (MMP), embryos were treated with 15 μM JC-10 dye (AAT Bioquest, Pleasanton, CA, USA) in M2 medium. Following incubation in the dark at 37°C for 30 min, the embryos were washed thrice with M2 medium. Red/green fluorescence signals were detected using a TCS SP5 confocal laser-scanning microscope (Leica), and fluorescence intensities were quantified using the ImageJ software. The average MMP of the embryos was determined by calculating the red fluorescence intensity (J-aggregates) to green fluorescence intensity (J-monomers) ratio. Each experimental group included approximately 10 embryos tested simultaneously, with four replicates for each group.

Caspase 3/7 apoptosis assay

To monitor caspase 3/7 activity, embryos were incubated with 8 μM Cell Event Caspase-3/7 (Thermo Fisher Scientific) in M2 medium. All embryos were stained in the dark at 37°C for 30 min. Subsequently, the embryos were fixed in 4% PFA for 15 min at room temperature. Then, DNA was counterstained with 25 μg/mL Hoechst 33342 (Sigma) for 10 min at room temperature. A TCS SP5 confocal laser scanning microscope (Leica) was used to detect fluorescent signals.

Statistical analysis

Tukey's Honestly Significant Difference test was used to assess significant differences in means between the three experimental groups, while the unpaired Student's *t*-test was used for comparisons between two experimental groups. Statistical analyses were conducted using the R software (Comprehensive R Archive Network, https://cran.r-project.org/). $P < 0.05$ was applied as the significance level for all tests.

Data availability

The RNA-seq data generated in this study have been submitted to the DDBJ Data Bank (https://www.ddbj.nig.ac.jp) under accession number, DRA017017.

Results

Effect of somatic mitochondria introduction on embryonic development

TEM revealed that as compared to liver-derived somatic mitochondria, zygotic mitochondria appeared rounder and smaller (Fig. 1A–C), and this is consistent with the findings of previous studies [9,10,32,33]. Following the introduction of somatic mitochondria into the perivitelline space, somatic mitochondria prepared for injection remained larger than zygotic mitochondria and possessed proper mitochondrial membrane and cristae structures (Fig. S1). Next, we observed mitochondria in mouse embryos into which somatic mitochondria had been injected using a glass pipette (SM-embryos). TEM analysis revealed a clear accumulation of injected presumptive somatic mitochondria in the SM-embryos (Fig. 1D and E), with somatic mitochondria preserving elongated structures and being larger than intrinsic zygotic mitochondria (Fig. 1F and G).

The developmental rates of SM-embryos were evaluated at 24–26 and 96–98 hpi, respectively. The proportions of two-cell embryos and blastocysts in SM-embryos were significantly lower than those of intact embryos and buffer-injected (BI) embryos ($P < 0.01$) (Table 1). Similarly, we introduced the zygotic mitochondria-enrichment cytoplasm (Fig. S2A-E) from another mouse embryo (ZM-embryos). ZM-embryos were prepared in a way that the amount of mitochondria observed in the bright field was equivalent to

that in SM-embryos (Fig. S2F and G). There were no significant differences in developmental rates between ZM-embryos and intact embryos (Table S6). By contrast, most SM-embryos showed cleavage arrest at the two-cell stage (Table 2). These findings indicate that the somatic mitochondria introduced into embryos maintained their morphological characteristics and contributed to cleavage arrest at the two-cell stage.

Disrupted zygotic gene activation in embryos with somatic mitochondria

To investigate the cause of arrest at the two-cell stage in SM-embryos, we focused on ZGA. Dynamic changes in gene expression associated with ZGA occur during the two-cell stage, and inhibition of ZGA has been associated with cleavage arrest at this developmental stage [34]. Initially, we determined the timing of the first embryonic cleavage in intact and SM-embryos using time-lapse imaging analyses as ZGA is closely linked to cell-cycle progression [35,36]. We observed that the first cleavage in SM embryos was delayed by approximately 3 hours compared to that in intact embryos (Fig. S3). Subsequently, we compared the transcriptomes of intact embryos collected between 32–33 hpi and SM embryos collected between 35–36 hpi using RNA-seq. Principal component analysis revealed distinct gene expression profiles between SM-embryos and intact embryos (Fig. 2A). We identified a total of 6,022 DEGs. A volcano plot demonstrated a more than two-fold upregulation in 3,144 genes, and a downregulation in 2,878 genes in SM embryos as compared to their expression levels in intact embryos ($P < 0.05$, Table S1, and Fig. 2B).

Among the DEGs, 230 major ZGA-related genes were identified using the transcriptome database for early mouse embryos (DBTMEE: http://dbtmee.hgc.jp/)

(Table S2). We further performed a clustering analysis of these genes and illustrated their expression levels in a heat map (Fig. 2C). The expression of major ZGA-related genes was significantly lower in SM-embryos than in intact embryos. Furthermore, we analyzed the mRNA expression levels of nine selected genes (*Glul, H2afz, Polr1c, Ppm1g, Mad2l1bp, Mcl1, Rpl18, Rps13,* and *Tceb2*) at the one-cell (10 hpi) and late two-cell (intact: 32 hpi, SM: 35 hpi) stages using qPCR. Seven out of the nine genes showed significant downregulation in SM-embryos ($P < 0.05$) (Fig. 2D). These results indicated that the introduction of somatic mitochondria into mouse embryos dysregulated major ZGA at the two-cell stage.

Subsequently, we investigated minor ZGA-related gene expression. Minor ZGA occurs before major ZGA and concludes before the initiation of major ZGA [35,37–39]. As with the major ZGA-related genes, we represented minor ZGA-related genes selected from among the DEGs in a heat map (Table S3 and Fig. 2E). Unlike major ZGA-related genes, most minor ZGA-related genes were upregulated in SM-embryos with respect to their expression in intact embryos. Furthermore, we analyzed the mRNA expression levels of the three selected minor ZGA-related genes (*Dux*, *MuERVL*, and *Zscan4*) in embryos at the one-cell and late two-cell stages using qPCR [37–39]. *Dux*, *MuERVL*, and *Zscan4* mRNA expression levels were significantly upregulated in SM-embryos ($P < 0.01$) (Fig. 2F). These findings indicated that the introduction of somatic mitochondria into early embryos dysregulated minor ZGA termination and the subsequent initiation of major ZGA, which is required for further embryonic development.

Histone modifications in mouse embryos with somatic mitochondria

We conducted immunostaining for SIRT1, an NAD^+-dependent protein deacetylase

used as a marker for ZGA [23,40]. The intensity of the SIRT1 signal in SM embryos was significantly lower than that in intact and BI embryos at the late two-cell stage ($P < 0.01$) (Fig. 3A and B). Given that SIRT1 is involved in histone modifications related to acetylation and demethylation [41,42], we examined acetylation of histone H3 at lysine 27 (H3K27ac) and trimethylation of histone H3 at lysine 4 (H3K4me3), respectively. There was an increase in H3K4me3 fluorescence signals (Fig. 3C and D) and a decrease in H3K27ac fluorescence signals (Fig. 3E and F) in SM embryos as compared to their signal intensities in intact and BI embryos at the late two-cell stage. These findings indicated that introducing somatic mitochondria into embryos disrupted histone modifications involving H3K27ac and H3K4me3, with a concomitant decrease in SIRT1 expression. These findings were supported by histone modifications and SIRT1 observations in embryos exposed to 2% dimethyl sulfoxide (DMSO), which also induces ZGA disruption and two-cell arrest (Fig. S4) [43].

Effects of somatic mitochondria introduction on NAD^+ levels

We evaluated intracellular NAD^+ levels in SM embryos as they are associated with SIRT1 activity [44] [45]. The NAD^+/NADH ratio in SM-embryos was significantly lower than that in intact and BI embryos at the two-cell stage ($P < 0.05$) (Fig. 4A and Table S7).

We further investigated the MMP in SM-embryos using JC-10 dye, as NAD^+ production depends on the MMP [45,46]. Introduced somatic mitochondria exhibited a higher MMP than endogenous zygotic mitochondria (Fig. 4B). At the two-cell stage, the MMP of SM embryos was significantly lower than that of intact and BI-embryos ($P < 0.05$) (Fig. 4C and D). These results demonstrated that somatic mitochondria introduction into early

embryos reduces MMP, resulting in a decrease in intracellular NAD^+ levels at the two-cell stage.

Introduction of somatic mitochondria into embryos induces apoptosis

ROS are produced by mitochondria and induce apoptosis by activating the caspase pathway [47,48]. We evaluated ROS levels using the fluorescent probe, CellROX™ Green Reagent. ROS levels in SM embryos were significantly higher than those in intact and BI embryos (Fig. 5A and B). In addition, through TEM analyses, vesicular/swollen mitochondria, typical of apoptotic cells, were observed in two-cell-stage SM-embryos (Fig. 5C-E) [49]. However, we could not confirm whether the vesicular/swollen mitochondria originated from injected somatic mitochondria or from intrinsic zygotic mitochondria. Next, we investigated cytochrome c release from mitochondria using immuno-TEM with anti-cytochrome c antibodies. In BI-embryos, cytochrome c was localized in the mitochondrial matrix surrounded by the inner membrane (Fig. 5F). In contrast, in SM-embryos, it was detected in both the mitochondrial and extramitochondrial compartments (Fig. 5G). Furthermore, we assessed caspase 3/7 activity in SM-embryos arrested at the two-cell stage using Cell Event Caspase 3/7, and detected significant fluorescence signals, indicating caspase 3/7 activation (Fig. 5H). These findings demonstrated that the introduction of somatic mitochondria into embryos resulted in cytochrome c release and caspase 3/7 activation, leading to apoptosis.

Discussion

ZGA inhibition results in developmental arrest at the two-cell stage [34,35]. However,

362 the regulatory effect of mitochondrial function on ZGA has not been comprehensively
363 investigated. In this study, liver-derived somatic mitochondria were introduced into
364 mouse embryos, and ZGA inhibition was observed. There are two types of ZGA, minor
365 and major ZGA. Stable expression of *Dux,* a minor ZGA-related gene, induces
366 developmental arrest at the two-cell stage [37–39]. In SM embryos, the expression
367 levels of minor ZGA genes, including *Dux,* remained high. Furthermore, suppression of
368 H3K4me3, which is required for the transition from minor to major ZGA [35,50], did not
369 occur in SM embryos (Fig. 3A and B). These results demonstrated that minor ZGA
370 termination, required for subsequent initiation of major ZGA, did not occur; thus, further
371 embryonic development was arrested in SM-embryos. Developmental arrest was
372 observed only in SM-embryos, and not in ZM-embryos (Table. 1 and Table. S6).
373 Although there are technical differences between SM- and ZM-embryos with respect to
374 the method of introduction of cytoplasmic material, it is highly unlikely that excess
375 mitochondria and/or these technical differences per se would critically affect the
376 development of micromanipulated embryos. This is because these have been
377 demonstrated in several previous studies on animal cloning and the rescue of defective
378 mouse, human, and pig oocytes [25,26,51–53]. Thus, the disrupted ZGA observed in
379 SM embryos is undoubtedly the consequence of somatic cell-derived mitochondria
380 introduction.
381 Mitochondria are dynamic cell organelles that divide and fuse repeatedly [54]. Like in
382 previous studies [25,27,28], the amount of mitochondria for introduction could not be
383 strictly defined; however, it was adjusted to be as equal as possible between SM- and
384 ZM-embryos in bright field. (Fig. S2F and G). SIRT1 expressed at the two-cell stage is
385 a ZGA marker [23,40], and is important for H3K27ac deacetylation and H3K4me3

386 demethylation [42]. Therefore, SIRT1 plays diverse roles in ZGA, and is responsible for
387 the termination of minor ZGA [41] and the transition from minor to major ZGA [35].
388 Decreased SIRT1 expression was observed in SM-embryos (Fig. 3E and F). This could
389 be due to a decrease in NAD^+ levels, as the NAD^+/NADH ratio decreased in SM
390 embryos (Fig. 4A). NAD^+ is a metabolic cofactor and a substrate for sirtuins (SIRTs),
391 which are involved in the maintenance of mitochondrial function [44]. As decreased
392 NAD^+ suppresses SIRT1 expression in rat bone marrow stem cells [55], it may also
393 lead to decreased SIRT1 expression in SM-embryos. NAD^+ is synthesized from NADH
394 through a redox reaction in mitochondrial complex I [56], depending on the
395 MMP[45,46]. We found a decrease in MMP in SM-embryos (Fig. 4C and D). These
396 findings suggested that in SM-embryos, mitochondrial dysfunction, including a
397 decrease in MMP, induces a deficiency in the synthesis of metabolites such as NAD^+;
398 this also prevents minor ZGA termination and major ZGA initiation by decreasing SIRT1
399 expression and disrupting histone modifications.
400 Somatic mitochondria exhibit a higher MMP than immature mitochondria in
401 undifferentiated cells [57]; therefore, metabolic activity differs between somatic cells
402 and early embryos [58]. As expected, we observed a regionally high MMP in SM
403 embryos immediately after mitochondrial injection (Fig. 4B). However, the introduction
404 of somatic mitochondria with higher MMP into the embryo did not increase MMP but
405 rather decreased it (Fig. 4C and D). This indicated a change in the homeostatic
406 balance in metabolic state in the SM-embryos. A low MMP may be necessary to
407 maintain genetic material stability in oocytes, as this suppresses ROS production and
408 DNA damage [59]. To restore the homeostatic balance disrupted by the introduction of
409 somatic mitochondria, the overall MMP within SM embryos might decrease, resulting in

410 an alteration of the metabolic state and an increase in ROS production. The
411 introduction of somatic mitochondria with higher MMP into the embryo did not lead to
412 an increase in overall MMP, but rather to a decrease in MMP. Thus, reducing MMP in
413 SM embryos may induce ZGA disruption.
414 In addition to the disruption in minor ZGA termination in SM embryos, major ZGA
415 initiation was also impaired. Major ZGA-associated genes were mostly downregulated
416 (Fig. 2C and D), and H3K27ac levels in SM-embryos decreased, with a concomitant
417 increase in H3K4me3 levels (Fig. 3C-F). Unexpectedly, there was a decrease in
418 H3K27ac levels in SM embryos as compared to its levels in intact and BI embryos, in
419 spite of the decrease in histone deacetylase and SIRT1 levels (Fig. 3A and B). Based
420 on this observation, we hypothesized that there might be a decrease in acetyl-CoA
421 availability in SM embryos. H3K27ac levels are dependent on intracellular acetyl-CoA
422 levels [60,61]; we speculated that there was also a decrease in acetyl-CoA levels in
423 SM-embryos. Acetyl-CoA is synthesized from pyruvate and acetate [61], and pyruvate
424 is transported into mitochondria through the pyruvate/H^+ symport system and then
425 converted into acetyl-CoA [62]. The MMP represents the H^+ transmembrane potential.
426 The decrease in MMP observed in SM-embryos correlates with decreased acetyl-CoA
427 levels. Moreover, acetyl-CoA synthesis from acetate requires ACSS2 deacetylation by
428 SIRT1 [63]. The decrease in NAD^+ and SIRT1 levels in SM embryos (Figures. 3A, B,
429 and 4A) might have contributed to the decrease in acetyl-CoA production. In addition,
430 ROS levels elevated in SM embryos inhibit SIRT1 activity and its degradation
431 [64].Therefore, our findings suggest that the disruption in major ZGA in SM-embryos
432 results from a dysregulation of histone modifications caused by decreased MMP and
433 decreased NAD^+ levels.

DUX overexpression and SIRT1 suppression induce the activation of the proapoptotic molecule, p53, resulting in the induction of apoptosis [65,66]. SIRT1 suppression prevented the termination of *Dux* downregulation-associated minor ZGA [41], which inhibited the transition from minor to major ZGA. Cytochrome c release and caspase3/7 activation were observed in SM-embryos (Fig. 5C-H). Our findings indicated that these apoptosis-inducing factors may inhibit the transition from minor to major ZGA in SM-embryos. Thus, developmental arrest of SM-embryos at the two-cell stage may be caused by the activation of apoptosis-inducing factors induced by the disruption in the transition from minor to major ZGA. Immediately after introduction, presumptive somatic mitochondria were not vacuolated nor swollen (Fig. 1E), and MMP remained high (Fig. 4B). These findings suggested that apoptosis was not induced by technical damage caused by microinjection but by a mismatch between the cell differentiation state and mitochondrial maturity.

This study demonstrates that the alignment between the cell differentiation state and mitochondrial maturity is crucial for transcriptional regulation through histone modifications. This mechanism holds significance for early embryonic development, as well as for cell survival and differentiation. Differentiated somatic cells with active OXPHOS retained well-developed mitochondria. In contrast, embryonic and induced pluripotent stem cells possess immature mitochondria [57,67]. Together with the cell differentiation state, mitochondrial morphological changes induce cell reprogramming and differentiation. For example, the induction of glycolysis and mitochondrial spheronization improves the efficiency of reprogramming induction [67–69]. Therefore, mitochondrial morphological and metabolic profiles appear to be universally important for achieving the properties of undifferentiated and differentiated cells [69]. In SM-

458 embryos, the introduced somatic mitochondria showed a morphology and size different
459 from those of the zygotes (Fig. 1F and G). This study shows that a mismatch between
460 the cell differentiation state and mitochondrial maturity in SM-embryos could disrupt
461 subsequent ZGA and induce developmental arrest at the two-cell stage.
462 However, we could not identify the factor(s) that caused the decrease in MMP. Hif1a, a
463 factor that promotes glycolysis through MMP suppression [70], could be associated
464 with this decrease in MMP in SM-embryos because *Hif1a* mRNA expression
465 significantly increased in these embryos as exemplified by the DEGs identified in the
466 RNA-seq data ($P < 0.05$) (Table S1). Further analysis of Hif1a in SM embryos did not
467 clarify how mitochondrial morphological transformation regulates developmental events
468 such as ZGA.
469 In conclusion, a mismatch between the cell differentiation state and mitochondrial
470 maturity led to metabolic changes and impaired mitochondrial function. This disruption
471 hindered the transition from minor to major ZGA by disrupting histone modifications,
472 resulting in mouse embryo arrest at the two-cell stage. Our findings suggest that
473 dynamically modifying mitochondrial morphology regulates transcription via epigenetic
474 modifications during early embryonic development. Thus, our study revealed the
475 involvement of embryonic mitochondria in ZGA regulation. Furthermore, the findings of
476 this study will contribute to improving our understanding of the significance of
477 mitochondrial remodeling in embryonic development across various species [71–73].
478 Mitochondrial supplementation has been proposed as a complementary treatment for
479 improving embryo competence [75–77]. However, the risks associated with introducing
480 mature mitochondria into the embryo were unclear. Our results indicated that
481 mitochondrial supplementation in assisted reproductive technologies should be more

carefully examined.

Acknowledgments

We thank Mr. Toshiaki Ito of the Electron Microscope Laboratory, Research Faculty of Agriculture, Hokkaido University, for providing expert advice on TEM analyses, and Ms. Fumi Yokoi of the Laboratory of Animal Genetics and Reproduction, Research Faculty of Agriculture, Hokkaido University, for assistance in the establishment of ZM-embryos. This study was funded by a grant-in-aid for Scientific Research (B) (24K01902) from the Ministry of Education, Culture, Sports, Science, and Technology of Japan.

Conflict of interest

The authors declare that they have no conflicts of interest with respect to the contents of this article.

Author contributions

Y.H. and M. K. designed the study; Y.H. performed the experiments and analyzed the data; H.B. and M.K. edited the manuscript; H.B., M.K. and M.T. collected samples; T.M. analyzed data; and Y.H. and M.K. wrote the paper.

References

[1] R Rizzuto, M Brini, M Murgia, T Pozzan. Microdomains with high Ca2+ close to IP3-sensitive channels that are sensed by neighboring mitochondria. Science. 1993; 262: 744-747.

[2] De Brito OM, Scorrano L. An intimate liaison: Spatial organization of the endoplasmic reticulum-mitochondria relationship. EMBO Journal 2010; 29:2715–2723.

[3] Vakifahmetoglu-Norberg H, Ouchida AT, Norberg E. The role of mitochondria in metabolism and cell death. Biochem Biophys Res Commun 2017; 482:426–431.
[4] Guo CY, Sun L, Chen XP, Zhang DS. Oxidative stress, mitochondrial damage and neurodegenerative diseases. Neural Regen Res 2013; 8:2003–2014.
[5] Bavister BD, Squirrell JM. Mitochondrial distribution and function in oocytes and early embryos. Hum. Reprod. 2000; 15: 189–198.
[6] Collins TJ, Berridge MJ, Lipp P, Bootman MD. Mitochondria are morphologically and functionally heterogeneous within cells. EMBO Journal 2002; 21:1616–1627.
[7] Motta PM, Nottola SA, Makabe S, Heyn R. Mitochondrial morphology in human fetal and adult female germ cells. Hum. Reprod. 2000; 15: 129–147.
[8] Sathananthan AH, Trounson AO. Mitochondrial morphology during preimplantational human embryogenesis. Hum. Reprod. 2000; 15: 148–159.
[9] Stern S, Biggers JD, Anderson E. Mitochondria and early development of the mouse. Journal of Experimental Zoology 1971; 176:179–191.
[10] Belli M, Zhang L, Liu X, Donjacour A, Ruggeri E, Palmerini MG, Nottola SA, MacChiarelli G, Rinaudo P. Oxygen concentration alters mitochondrial structure and function in in vitro fertilized preimplantation mouse embryos. Human Reproduction 2019; 34:601–611.
[11] Plante L, King WA. Light and electron microscopic analysis of bovine embryos derived by in Vitro and in Vivo fertilization. J Assist Reprod Genet 1994; 11:515–529.
[12] Kumar RP, Ray S, Home P, Saha B, Bhattacharya B, Wilkins HM, Chavan H, Ganguly A, Milano-Foster J, Paul A, Krishnamurthy P, Swerdlow RH, et al. Regulation of energy metabolism during early mammalian development: Tead4 controls mitochondrial transcription. Development 2018; 145: dev.162644.
[13] Hayashi Y, Saito S, Bai H, Takahashi M, Kawahara M. Mitochondrial maturation in the trophectoderm and inner cell mass. Theriogenology 2021; 175: 69–76.
[14] Mishra P, Chan DC. Metabolic regulation of mitochondrial dynamics. Journal of Cell Biology 2016; 212:379–387.
[15] Cogliati S, Enriquez JA, Scorrano L. Mitochondrial Cristae: Where Beauty Meets Functionality. Trends Biochem Sci 2016; 41:261–273.
[16] Tondera D, Grandemange S, Jourdain A, Karbowski M, Mattenberger Y, Herzig S, Da Cruz S, Clerc P, Raschke I, Merkwirth C, Ehses S, Krause F, et al. SlP-2 is required for stress-induced mitochondrial hyperfusion. EMBO Journal 2009; 28:1589–1600.
[17] Shi P, Ren X, Meng J, Kang C, Wu Y, Rong Y, Zhao S, Jiang Z, Liang L, He W, Yin

Y, Li X, et al. Mechanical instability generated by Myosin 19 contributes to mitochondria cristae architecture and OXPHOS. Nat Commun. 2022; 13: 2673.

[18] Houghton FD. Energy metabolism of the inner cell mass and trophectoderm of the mouse blastocyst. Differentiation 2006; 74:11–18.

[19] Hom JR, Quintanilla RA, Hoffman DL, de Mesy Bentley KL, Molkentin JD, Sheu SS, Porter GA. The permeability transition pore controls cardiac mitochondrial maturation and myocyte differentiation. Dev Cell 2011; 21:469–478.

[20] Dai DF, Danoviz ME, Wiczer B, Laflamme MA, Tian R. Mitochondrial maturation in human pluripotent stem cell derived cardiomyocytes. Stem Cells Int 2017; 2017: 5153625.

[21] Charmpilas N, Tavernarakis N. Mitochondrial maturation drives germline stem cell differentiation in Caenorhabditis elegans. Cell Death Differ 2020; 27:601–617.

[22] Sharpley MS, Chi F, Hoeve J ten, Banerjee U. Metabolic plasticity drives development during mammalian embryogenesis. Dev Cell 2021; 56:2329-2347.

[23] Nagaraj R, Sharpley MS, Chi F, Braas D, Zhou Y, Kim R, Clark AT, Banerjee U. Nuclear localization of mitochondrial TCA cycle enzymes as a critical step in mammalian zygotic genome activation. Cell 2017; 168:210-223.

[24] Yamazaki W, Amano T, Bai H, Takahashi M, Kawahara M. The influence of polyploidy and genome composition on genomic imprinting in mice. Journal of Biological Chemistry 2016; 291:20924–20931.

[25] Takeda K, Tasai M, Iwamoto M, Onishi A, Tagami T, Nirasawa K, Hanada H, Pinkert CA. Microinjection of cytoplasm or mitochondria derived from somatic cells affects parthenogenetic development of murine oocytes. Biol Reprod 2005; 72:1397–1404.

[26] Cagnone GLM, Tsai TS, Makanji Y, Matthews P, Gould J, Bonkowski MS, Elgass KD, Wong ASA, Wu LE, McKenzie M, Sinclair DA, John JCS. Restoration of normal embryogenesis by mitochondrial supplementation in pig oocytes exhibiting mitochondrial DNA deficiency. Sci Rep 2016; 6:27–31

[27] Rt E, Irwi N MH, Moffatt RJ. Mitochondria transfer into mouse ova by microinjection. Transgenic Res 1997;6:379-83.

[28] Yi YC, Chen MJ, Ho JYP, Guu HF, Ho ESC. Mitochondria transfer can enhance the murine embryo development. J Assist Reprod Genet 2007; 24:445–449.

[29] Akizawa H, Kobayashi K, Bai H, Takahashi M, Kagawa S, Nagatomo H, Kawahara M. Reciprocal regulation of TEAD4 and CCN2 for the trophectoderm development of the bovine blastocyst Reproduction 2018; 155: 563-571.

[30] Gwatkin RBL. Effect of enzymes and acidity on the zona pellucida of the mouse

egg before and after fertilization. J Reprod Fertil; 1964; 7:99-105.

[31] Follet-Gueye M-L, Pagny S, Faye L, Gomord V, Driouich A. An Improved Chemical Fixation Method Suitable for Immunogold Localization of Green Fluorescent Protein in the Golgi Apparatus of Tobacco Bright Yellow (BY-2) Cells. J Histochem Cytochem 2003; 51: 931-940.

[32] J E Klaunig, P J Goldblatt, D E Hinton, M M Lipsky, J Chacko, B F Trump. Mouse liver cell culture. I. Hepatocyte isolation. In Vitro 1981; 17:913–925.

[33] Irina G. Shabalina, Mikhail Yu. Vyssokikh, Natalia Gibanova, Robert I. Csikasz, Daniel Edgar, Anne Hallden-Waldemarson, Zinaida Rozhdestvenskaya, Lora E. Bakeeva, Valeria B. Vays, Antonina V. Pustovidko, Maxim V. Skulachev, Barbara Cannon, et al. Improved health-span and lifespan in mtDNA mutator mice treated with the mitochondrially targeted antioxidant SkQ1. Aging 2017; 9:315–336.

[34] CM Warner, LR Versteegh. In vivo and in vitro effect of α-amanitin on preimplantation mouse embryo RNA polymerase. Nature 1974; 248:678–680.

[35] Abe K ichiro, Funaya S, Tsukioka D, Kawamura M, Suzuki Y, Suzuki MG, Schultz RM, Aoki F. Minor zygotic gene activation is essential for mouse preimplantation development. Proc Natl Acad Sci U S A 2018; 115:E6780–E6788.

[36] Aoki F, Worrad DM, Schultz RM. Regulation of transcriptional activity during the first and second cell cycles in the preimplantation mouse embryo. Dev Biol 1997; 181: 296-307.

[37] Sugie K, Funaya S, Kawamura M, Nakamura T, Suzuki MG, Aoki F. Expression of Dux family genes in early preimplantation embryos. Sci Rep 2020; 10: 1939.

[38] Percharde M, Lin CJ, Yin Y, Guan J, Peixoto GA, Bulut-Karslioglu A, Biechele S, Huang B, Shen X, Ramalho-Santos M. A LINE1-Nucleolin partnership regulates early development and ESC Identity. Cell 2018; 174:391-405.e19.

[39] Guo M, Zhang Y, Zhou J, Bi Y, Xu J, Xu C, Kou X, Zhao Y, Li Y, Tu Z, Liu K, Lin J, et al. Precise temporal regulation of Dux is important for embryo development. Cell Res 2019; 29:956–959.

[40] Gambini A, Stein P, Savy V, Grow EJ, Papas BN, Zhang Y, Kenan AC, Padilla-Banks E, Cairns BR, Williams CJ. Developmentally programmed tankyrase activity upregulates β-Catenin and licenses progression of embryonic genome activation. Dev Cell 2020; 53:545-560.

[41] Li J, Zhang J, Hou W, Yang X, Liu X, Zhang Y, Gao M, Zong M, Dong Z, Liu Z, Shen J, Cong W, et al. Metabolic control of histone acetylation for precise and timely regulation of minor ZGA in early mammalian embryos. Cell Discov 2022; 8:

96.

[42] Xing X, Zhang J, Wu T, Zhang J, Wang Y, Su J, Zhang Y. SIRT1 reduces epigenetic and non-epigenetic changes to maintain the quality of postovulatory aged oocytes in mice. Exp Cell Res 2021; 399: 112421.

[43] Kang MH, You SY, Hong K, Kim JH. DMSO impairs the transcriptional program for maternal-to-embryonic transition by altering histone acetylation. Biomaterials 2020; 230: 119604.

[44] Haigis MC, Sinclair DA. Mammalian sirtuins: Biological insights and disease relevance. Annual Review of Pathology: Mechanisms of Disease 2010; 5:253–295.

[45] Yang Q, Cong L, Wang Y, Luo X, Li H, Wang H, Zhu J, Dai S, Jin H, Yao G, Shi S, Hsueh AJ, et al. Increasing ovarian NAD+ levels improve mitochondrial functions and reverse ovarian aging. Free Radic Biol Med 2020; 156:1–10.

[46] Li X, Wang X, Zhang C, Wang J, Wang S, Hu L. Dysfunction of metabolic activity of bone marrow mesenchymal stem cells in aged mice. Cell Prolif 2022; 55: e13191.

[47] Redza-Dutordoir M, Averill-Bates DA. Activation of apoptosis signalling pathways by reactive oxygen species. Biochim Biophys Acta Mol Cell Res 2016; 1863:2977–2992.

[48] Garrido C, Galluzzi L, Brunet M, Puig PE, Didelot C, Kroemer G. Mechanisms of cytochrome c release from mitochondria. Cell Death Differ 2006; 13:1423–1433.

[49] Sun MG, Williams J, Munoz-Pinedo C, Perkins GA, Brown JM, Ellisman MH, Green DR, Frey TG. Correlated three-dimensional light and electron microscopy reveals transformation of mitochondria during apoptosis. Nat Cell Biol 2007; 9:1057–1065.

[50] Dahl JA, Jung I, Aanes H, Greggains GD, Manaf A, Lerdrup M, Li G, Kuan S, Li B, Lee AY, Preissl S, Jermstad I, et al. Broad histone H3K4me3 domains in mouse oocytes modulate maternal-to-zygotic transition. Nature 2016; 537:548–552.

[51] Sayaka W, Satoshi K, Van Thuan N, Hiroshi O, Takafusa H, Eiji M, Thuy BH, Masashi M, Teruhiko W. Effect of volume of oocyte cytoplasm on embryo development after parthenogenetic activation, intracytoplasmic sperm injection, or somatic cell nuclear transfer. Zygote 2008; 16:211–222.

[52] Van Thuan N, Wakayama S, Kishigami S, Ohta H, Hikichi T, Mizutani E, Bui HT, Wakayama T. Injection of somatic cell cytoplasm into oocytes before intracytoplasmic sperm injection impairs full-term development and increases placental weight in mice. Biol Reprod 2006; 74:865–873.

[53] Huang C-C, Cheng T-C, Chang H-H, Chang C-C, Chen C-I, Liu J, Lee M-S. Birth after the injection of sperm and the cytoplasm of tripronucleate zygotes into metaphase II oocytes in patients with repeated implantation failure after assisted fertilization procedures. Fertil Steril. 1999; 72, 702-706.

[54] Chang CR, Blackstone C. Dynamic regulation of mitochondrial fission through modification of the dynamin-related protein Drp1. Annals of the New York Academy of Sciences, vol. 1201. Blackwell Publishing Inc.; 2010:34–39.

[55] Ma C, Pi C, Yang Y, Lin L, Shi Y, Li Y, Li Y, He X. Nampt expression decreases age-related senescence in rat bone marrow mesenchymal stem cells by targeting Sirt1. PLoS One 2017; 12: e0170930.

[56] Yin B, Zhang J, Liu Y, Pan X, Zhao Z, Li H, Zhang C, Li C, Du X, Li Y, Liu D, Lu H. PtomtAPX, a mitochondrial ascorbate peroxidase, plays an important role in maintaining the redox balance of Populus tomentosa Carr. Sci Rep 2019; 9: 19541.

[57] Cho YM, Kwon S, Pak YK, Seol HW, Choi YM, Park DJ, Park KS, Lee HK. Dynamic changes in mitochondrial biogenesis and antioxidant enzymes during the spontaneous differentiation of human embryonic stem cells. Biochem Biophys Res Commun 2006; 348:1472–1478.

[58] Lees JG, Gardner DK, Harvey AJ. Pluripotent stem cell metabolism and mitochondria: beyond ATP. Stem Cells Int 2017; 2017: 2874283.

[59] Rodríguez-Nuevo A, Torres-Sanchez A, Duran JM, De Guirior C, Martínez-Zamora MA, Böke E. Oocytes maintain ROS-free mitochondrial metabolism by suppressing complex I. Nature 2022; 607:756–761.

[60] Lee J V., Carrer A, Shah S, Snyder NW, Wei S, Venneti S, Worth AJ, Yuan ZF, Lim HW, Liu S, Jackson E, Aiello NM, et al. Akt-dependent metabolic reprogramming regulates tumor cell Histone acetylation. Cell Metab 2014; 20:306–319.

[61] Sivanand S, Viney I, Wellen KE. Spatiotemporal Control of Acetyl-CoA Metabolism in Chromatin Regulation. Trends Biochem Sci 2018; 43:61–74.

[62] McCommis KS, Finck BN. Mitochondrial pyruvate transport: A historical perspective and future research directions. Biochemical Journal 2015; 466:443–454.

[63] Yi Wu, Yang Liu, Zhihong Hao, Xingguo Liu. NAD + is critical for maintaining acetyl-CoA and H3K27ac in embryonic stem cells by Sirt1-dependent deacetylation of AceCS1. vol. 1. 2022.

[64] Chen Z, Shentu TP, Wen L, Johnson DA, Shyy JYJ. Regulation of SIRT1 by oxidative stress-responsive miRNAs and a systematic approach to identify its role in the endothelium. Antioxid Redox Signal 2013; 19:1522–1538.

[65] Eidahl JO, Giesige CR, Domire JS, Wallace LM, Fowler AM, Guckes SM, Garwick-Coppens SE, Labhart P, Harper SQ. Mouse Dux is myotoxic and shares partial functional homology with its human paralog DUX4. Hum Mol Genet 2016; 25:4577–4589.

[66] Luo J, Nikolaev AY, Imai S, Chen D, Su F, Shiloh A, Guarente L, Gu W. Signifi. Cell. 2001; 107, 137-148.

[67] Folmes CDL, Nelson TJ, Martinez-Fernandez A, Arrell DK, Lindor JZ, Dzeja PP, Ikeda Y, Perez-Terzic C, Terzic A. Somatic oxidative bioenergetics transitions into pluripotency-dependent glycolysis to facilitate nuclear reprogramming. Cell Metab 2011; 14:264–271.

[68] Son MY, Choi H, Han YM, Cho YS. Unveiling the critical role of REX1 in the regulation of human stem cell pluripotency. Stem Cells 2013; 31:2374–2387.

[69] Wanet A, Arnould T, Najimi M, Renard P. Connecting Mitochondria, Metabolism, and Stem Cell Fate. Stem Cells Dev 2015; 24:1957–1971.

[70] Nicholas C. Denko. Hypoxia, HIF1 and glucose metabolism in the solid tumour. Nat Rev Cancer 2008; 8:705–713.

[71] Thouas GA, Trounson AO, Wolvetang EJ, Jones GM. Mitochondrial dysfunction in mouse oocytes results in preimplantation embryo arrest in vitro. Biol Reprod 2004; 71:1936–1942.

[72] Stojkovic M, Machado SA, Stojkovic P, Zakhartchenko V, Hutzler P, Gonçalves PB, Wolf E. Mitochondrial distribution and adenosine triphosphate content of bovine oocytes before and after in vitro maturation: correlation with morphological criteria and developmental capacity after in vitro fertilization and culture. Biol Reprod. 2001; 64: 904-909.

[73] Van Blerkom J. Mitochondrial function in the human oocyte and embryo and their role in developmental competence. Mitochondrion 2011; 11:797–813.

Figure legends

Figure 1. Ultrastructure of mitochondria in mouse zygotes injected with somatic mitochondria

A, B) Mitochondrial ultrastructure in intact zygotes. Magnification × 40,000 (A) and × 60,000 (B), Scale bar = 500 nm (A) and 200 nm (B). C) Mitochondrial ultrastructure in

liver tissue cells. Magnification × 40,000, Scale bar = 500 nm. D) Presumptive somatic mitochondria-injected embryo (SM-embryo) at the zygote stage. Magnification × 1,500. Scale bar = 10 μm. E) An enlarged view of the frame in (D). Magnification × 6,000, Scale bar = 2 μm. F) Enlarged view of the left frame in (E). Magnification × 20,000, Scale bar = 1 μm. Arrow: presumptive somatic cell mitochondria; Arrowhead: zygotic mitochondria. G) Enlarged view of the right frame in (E). Magnification × 60,000, Scale bar = 200 nm.

Figure 2. Disruption of zygotic gene activation in embryos with somatic mitochondria

A) Principal component analysis plot for all genes across all samples; somatic mitochondria-injected embryos (SM-embryos) exhibited distinct gene expression profiles and are separated from intact embryos based on PC1. B) Volcano plot showing differentially expressed genes between SM-embryos and intact embryos. A Padj < 0.05 was considered statistically significant and is represented by a dashed line indicating the logarithmic value. Significantly up- and downregulated genes are highlighted in red and green, respectively. Genes with no significant differential expression are indicated in blue. C) Hierarchical clustering analysis for 230 major zygotic gene activation (ZGA)-related genes. D) Log-ratio (late two-cell/one-cell) for the relative expression levels of nine selected genes. E) Hierarchical clustering analysis for 233 minor ZGA-related genes. F) Log-ratio (late two-cell/one-cell) for the relative expression levels of three selected genes. (**: $P < 0.01$, *: $P < 0.05$). Late two-cell stage- Intact: 32–33 hpi; SM: 35–36 hpi. one-cell stage: 10 hpi. hpi: hours post-insemination.

Figure 3. Alterations in histone modifications in embryos with somatic mitochondria

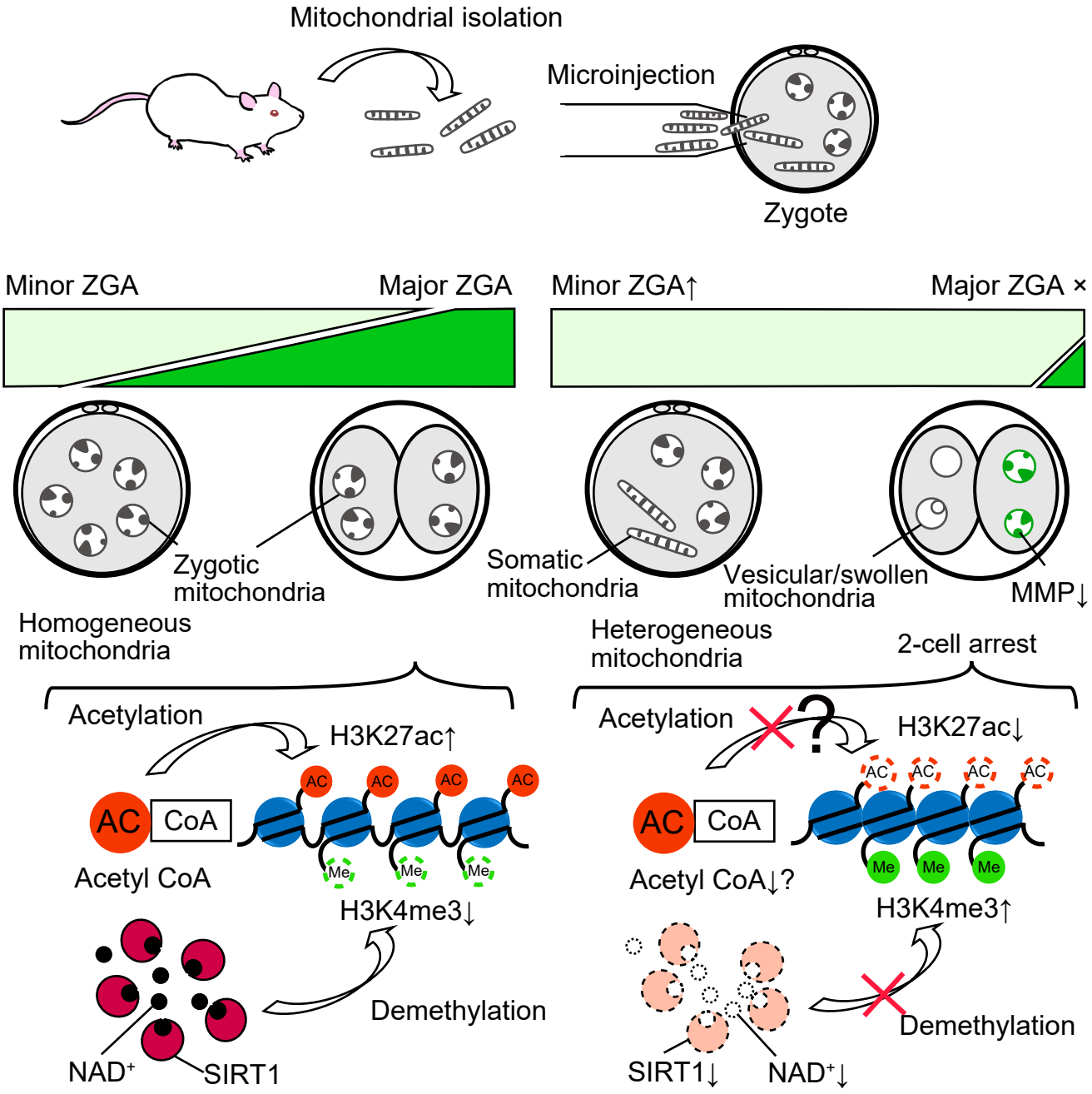
A) Immunofluorescence detection of SIRT1 in late two-cell-stage embryos. Scale bars = 25 μm. B) $P < 0.01$ (nuclei n > 30) for comparison of nuclear signal intensity. Black lines indicate average signal intensities Approximately seven embryos were simultaneously tested, with three replicates for each group. C) Immunofluorescence detection of H3K4 trimethylation in late two-cell-stage embryos. BI: buffer-injected embryo. SM: somatic mitochondria-injected embryo. Scale bars = 25 μm. D) $P < 0.01$ (nuclei n > 50) for comparison of nuclear signal intensity. Black lines indicate average signal intensities. Approximately seven embryos were simultaneously tested, with four replicates for each group. E) Immunofluorescence detection of H3K27 acetylation in late two-cell-stage embryos. Scale bars = 25 μm. F) $P < 0.01$ (nuclei n > 40) for comparison of nuclear signal intensity. Black lines indicate average signal intensities. Approximately seven embryos were simultaneously tested, with three replicates for each group.

Figure 4. Alterations in metabolite levels and mitochondrial membrane potential in embryos with somatic mitochondria

A) NAD^+/NADH ratios in 20 embryos (n = 4 replicates). Black lines indicate average NAD^+/NADH ratios (Intact: 0.54; BI: 0.51; and SM: 0.44). Different letters indicate statistically significant differences ($P < 0.05$). B) Representative images of one-cell-stage embryos stained with JC-10 dye. Green and red fluorescence indicate JC-10 monomers and aggregates, respectively. Arrowhead: Injected presumptive somatic mitochondria. Scale bars = 50 μm. C) Representative images of two-cell-stage

770 embryos stained with JC-10 dye. Scale bars = 50 μm. (D) $P < 0.05$ (embryo n > 35) for
771 comparison of the embryo signal intensity ratio (red/green). Black lines indicate
772 average signal intensity ratios. Approximately 10 embryos were simultaneously tested,
773 with four replicates for each group.
774
775 **Figure 5. Apoptosis in somatic mitochondria-injected embryos**
776 A) Fluorescence micrograph showing intracellular ROS levels in two-cell-stage
777 embryos through staining with CellROX™ Green Reagent. Scale bars = 25 μm. B) $P <$
778 0.05 (embryo n > 14) for comparison of the embryo signal intensity. Black lines indicate
779 average signal intensities. Approximately five embryos were simultaneously tested,
780 with three replicates for each group. C) Mitochondrial ultrastructure in two-cell-stage
781 buffer-injected embryos (BI-embryo). Magnification × 40.000, Scale bar = 500 μm. D,
782 E) Mitochondrial ultrastructure in two-cell-stage somatic mitochondria-injected embryos
783 (SM-embryo). Magnification × 40,000 (D) and × 80,000 (E), Scale bar = 500 μm (D)
784 and 200 μm (E). Arrowhead = vesicular/swollen mitochondrion. F) Immuno-
785 transmission electron microscopic (TEM) image showing cytochrome c within a
786 mitochondrion in a BI-embryo. Red arrowheads: cytochrome c signals within
787 mitochondrion; Yellow arrowheads: cytochrome c signals outside of mitochondrion.
788 Magnification × 50,000, Scale bar = 500 μm. G) Immuno-TEM image showing
789 cytochrome c out of mitochondrion in SM-embryos. Red arrowheads: cytochrome c
790 signals within mitochondrion; Yellow arrowheads: cytochrome c signals outside of
791 mitochondrion. Magnification × 50,000, Scale bar = 500 μm. H) Fluorescence
792 micrograph showing the effect of somatic mitochondria introduction on the caspase
793 pathway through staining with the CellEvent Caspase-3/7 Green Detection Reagent.

794 Scale bars = 50 μm.


Mitochondrial isolation
Microinjection
Zygote
Minor ZGA
Major ZGA
Minor ZGA↑
Major ZGA ×
Zygotic mitochondria
Somatic mitochondria
Vesicular/swollen mitochondria
MMP↓
Homogeneous mitochondria
Heterogeneous mitochondria
2-cell arrest
Acetylation
H3K27ac↑
AC
CoA
Acetyl CoA
Me
H3K4me3↓
Demethylation
NAD⁺
SIRT1
Acetylation
?
H3K27ac↓
Acetyl CoA↓?
H3K4me3↑
Demethylation
SIRT1↓
NAD⁺↓

Tables

Table 1. Developmental rates of embryos after the introduction of somatic mitochondria

	No. of embryos examined	No. of two-cell-stage embryos at 24–26 hpi (% ± SEM)	No. of blastocysts at 96–98 hpi (% ± SEM)
Intact embryos	162	154 (95.2 ± 6.5)^{a}	132 (82.0 ± 7.4)$^{\mathrm{A}}$
BI-embryos	160	152 (95.1 ± 4.8)^{a}	115 (72.8 ± 11.1)$^{\mathrm{A}}$
SM-embryos	201	98 (48.8 ± 25.7)$^{\mathrm{b}}$	18 (8.8 ± 9.5)$^{\mathrm{B}}$

Hpi, hours post-insemination; SEM: standard error of the mean; BI: buffer-injected; SM: somatic mitochondria-injected. Different letters indicate statistically significant differences ($P < 0.01$). n = 9 or 10 replicates.

Table 2. Developmental rates of embryos following the introduction of somatic mitochondria after the two-cell stage

	No. of embryos examined	No. of two-cell-stage embryos at 24–26 hpi (% ± SEM)	No. of 3–4-cell-stage embryos at 44–46 hpi (% ± SEM)
Intact embryos	41	40 (97.6 ± 2.8)^{a}	31 (75.6 ± 14.6)$^{\mathrm{A}}$
BI-embryos	30	29 (96.7 ± 3.0)^{a}	24 (80.0 ± 13.7)$^{\mathrm{A}}$
SM-embryos	100	55 (55.0 ± 10.8)$^{\mathrm{b}}$	4 (4.0 ± 1.7)$^{\mathrm{B}}$

Hpi, hours post-insemination; SEM: standard error of the mean; BI: buffer-injected; SM: somatic mitochondria-injected. Different letters indicate statistically significant differences ($P < 0.01$). n = 3 or 4 replicates.

Fig.1

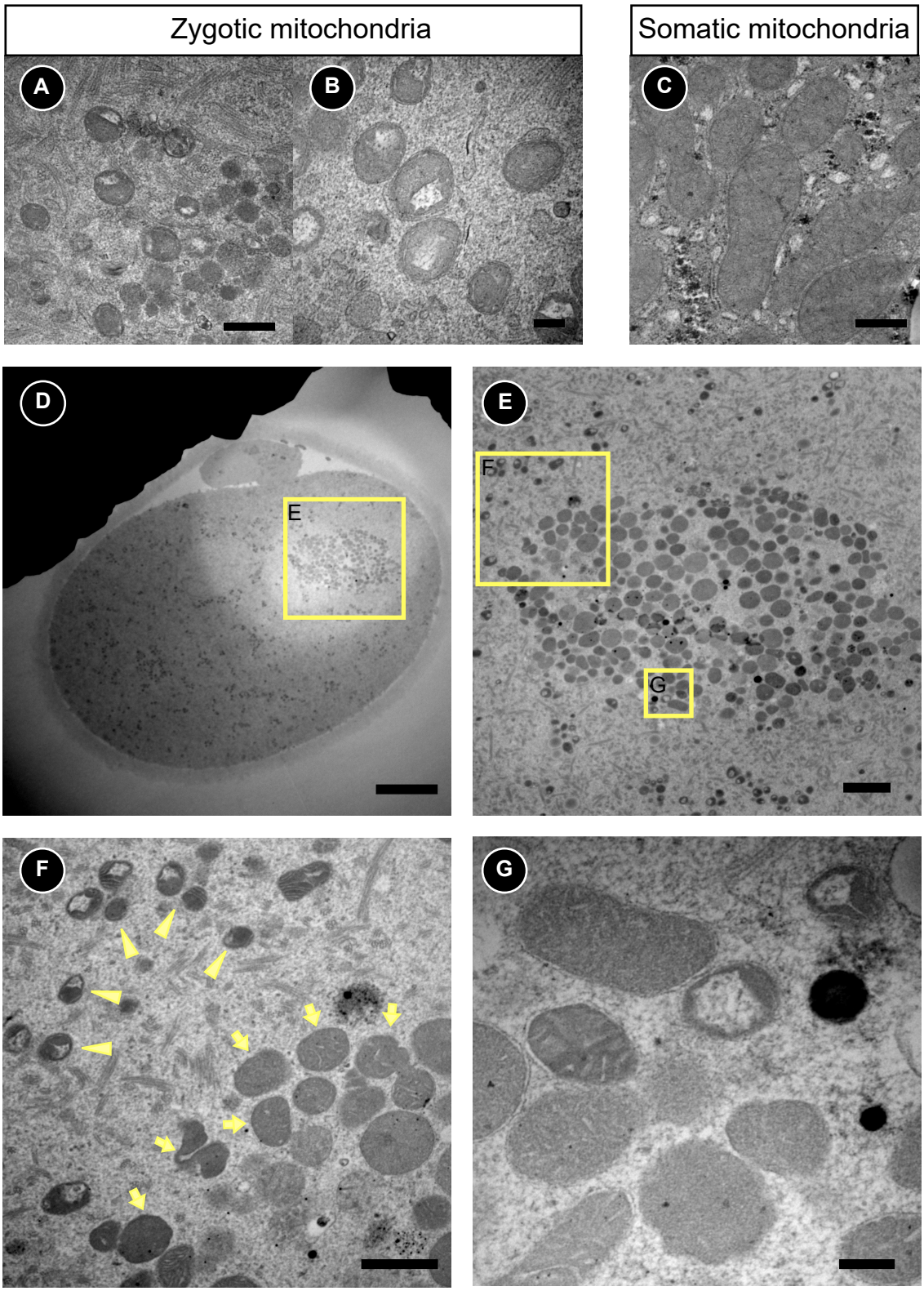


Fig.2

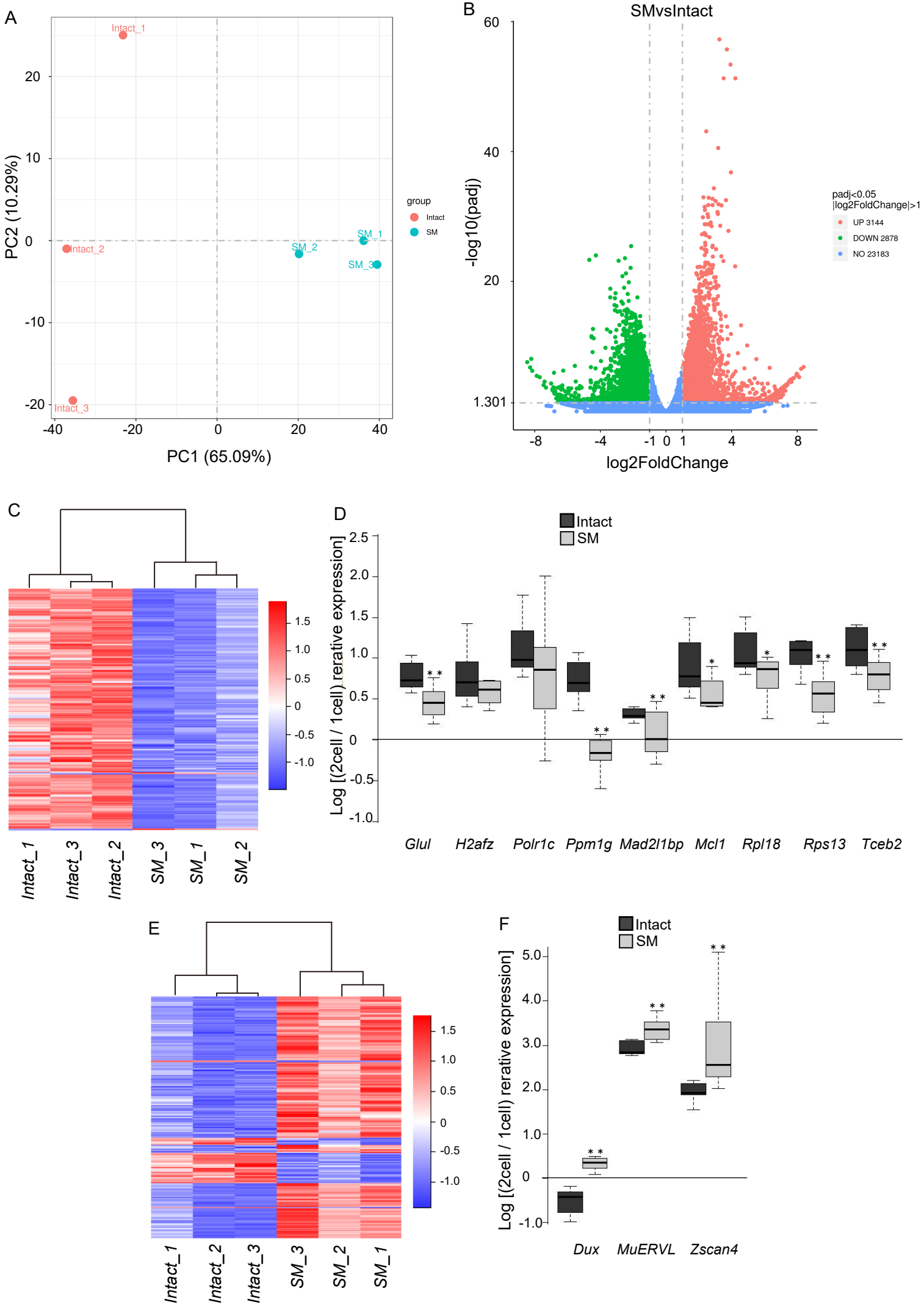

A
Intact_1
Intact_2
Intact_3
SM_1
SM_2
SM_3
PC1 (65.09%)
PC2 (10.29%)
group
Intact
SM
B
SMvsIntact
-log10(padj)
log2FoldChange
padj<0.05
|log2FoldChange|>1
UP 3144
DOWN 2878
NO 23183
C
Intact_1
Intact_3
Intact_2
SM_3
SM_1
SM_2
D
Intact
SM
Log [(2cell / 1cell) rerative expression]
Glul
H2afz
Polr1c
Ppm1g
Mad2l1bp
Mcl1
Rpl18
Rps13
Tceb2
E
Intact_1
Intact_2
Intact_3
SM_3
SM_2
SM_1
F
Intact
SM
Log [(2cell / 1cell) rerative expression]
Dux
MuERVL
Zscan4

Fig. 3

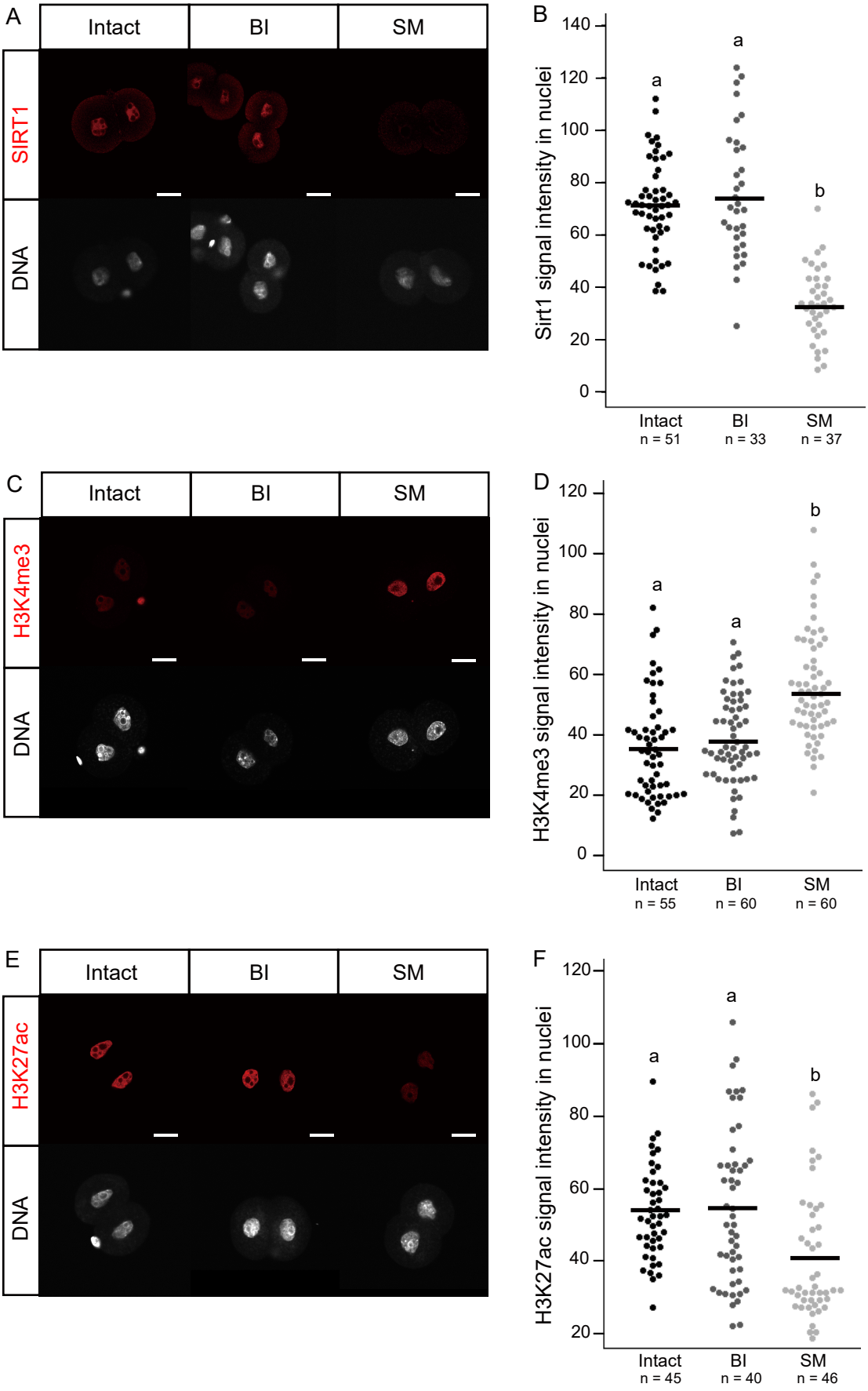

A
Intact
BI
SM
SIRT1
DNA
B
Sirt1 signal intensity in nuclei
140
120
100
80
60
40
20
0
a
a
b
Intact
n = 51
BI
n = 33
SM
n = 37
C
Intact
BI
SM
H3K4me3
DNA
D
H3K4me3 signal intensity in nuclei
120
100
80
60
40
20
0
a
a
b
Intact
n = 55
BI
n = 60
SM
n = 60
E
Intact
BI
SM
H3K27ac
DNA
F
H3K27ac signal intensity in nuclei
120
100
80
60
40
20
a
a
b
Intact
n = 45
BI
n = 40
SM
n = 46

Fig.4

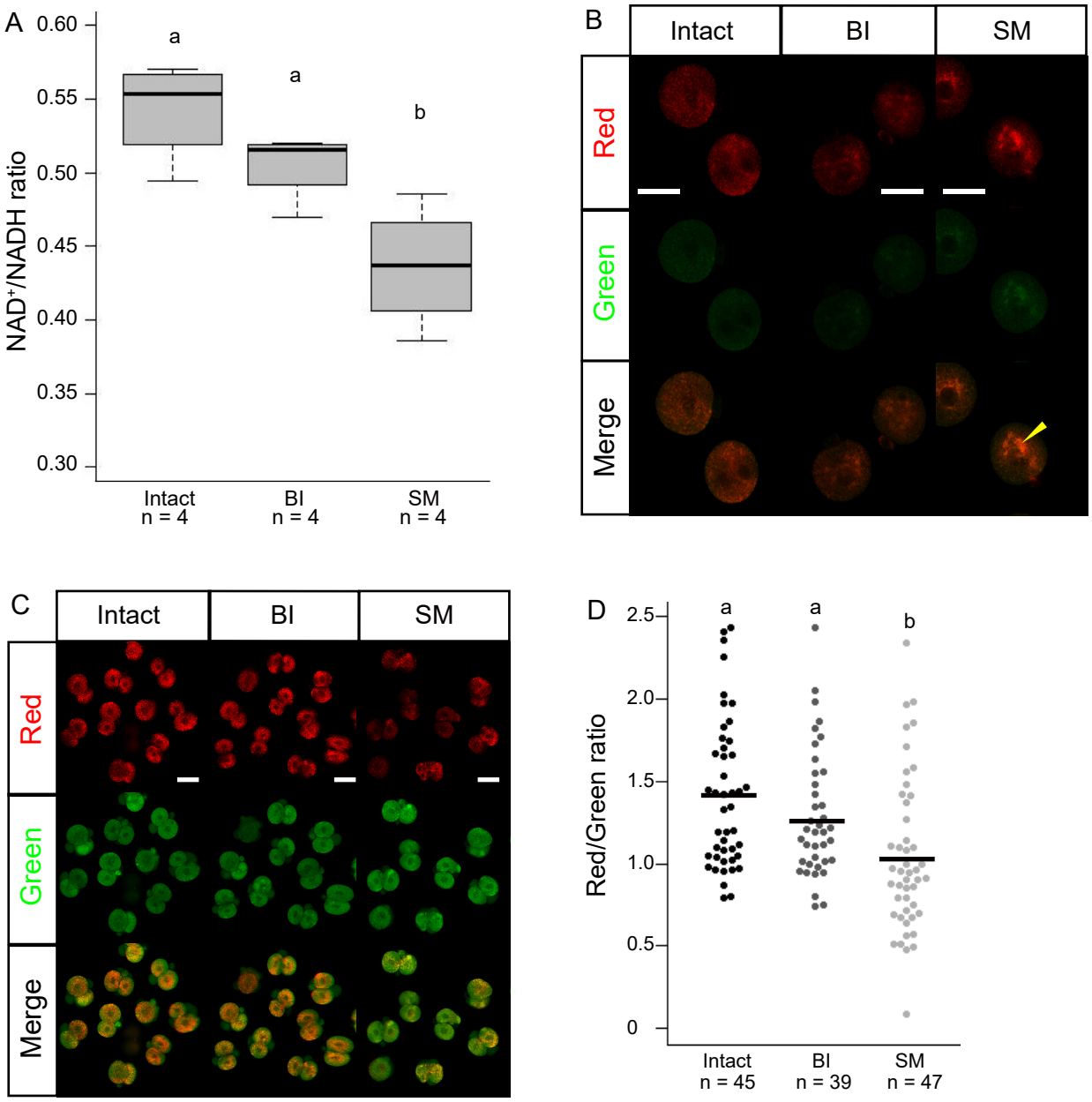

A
NAD+/NADH ratio
0.60
0.55
0.50
0.45
0.40
0.35
0.30
a
a
b
Intact
n = 4
BI
n = 4
SM
n = 4
B
Intact
BI
SM
Red
Green
Merge
C
Intact
BI
SM
Red
Green
Merge
D
Red/Green ratio
2.5
2.0
1.5
1.0
0.5
0
a
a
b
Intact
n = 45
BI
n = 39
SM
n = 47

Fig.5

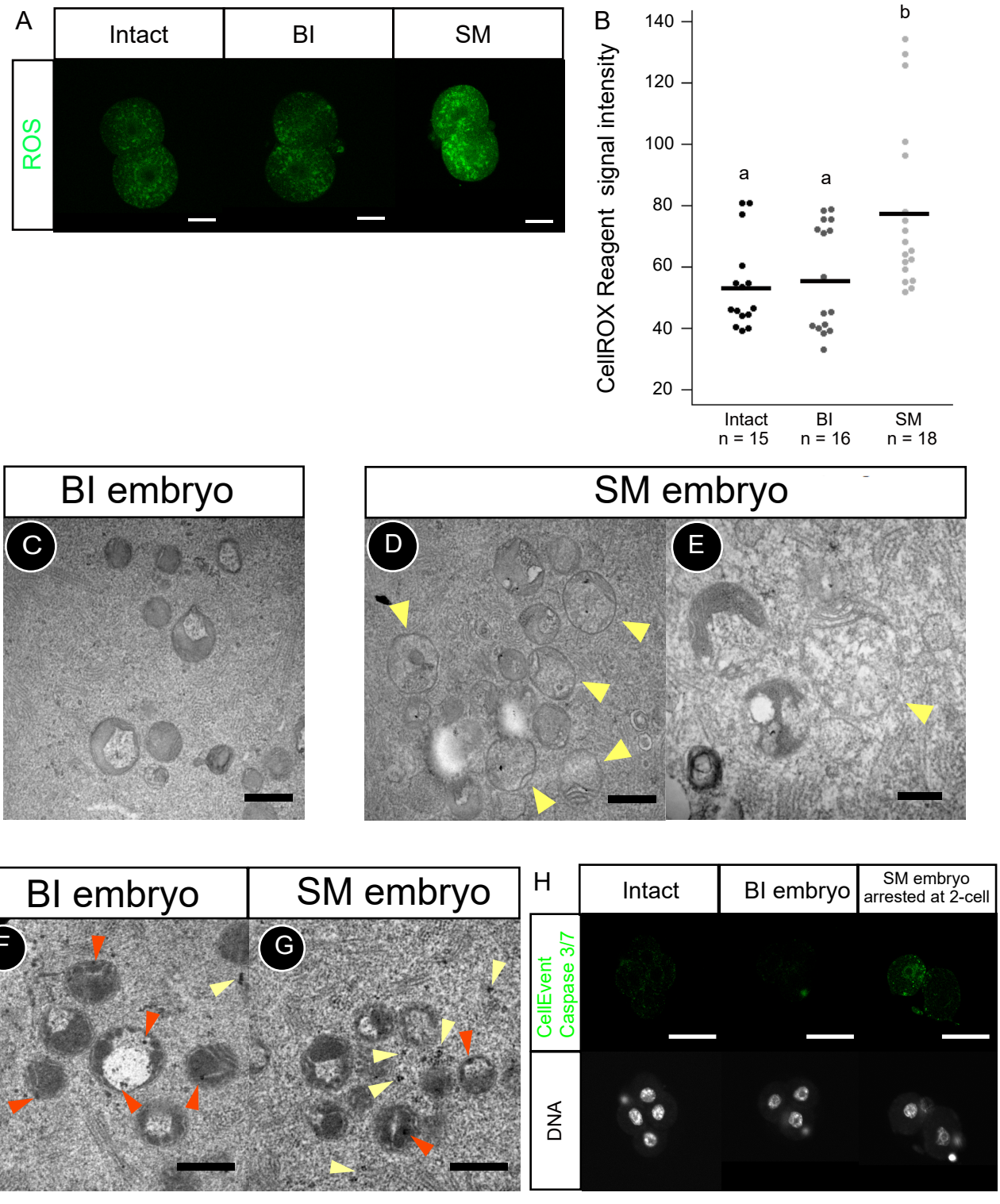

A
Intact
BI
SM
ROS
B
CellROX Reagent signal intensity
140
120
100
80
60
40
20
a
a
b
Intact
n = 15
BI
n = 16
SM
n = 18
BI embryo
SM embryo
C
D
E
BI embryo
SM embryo
F
G
H
Intact
BI embryo
SM embryo
arrested at 2-cell
CellEvent
Caspase 3/7
DNA

Fig.S1

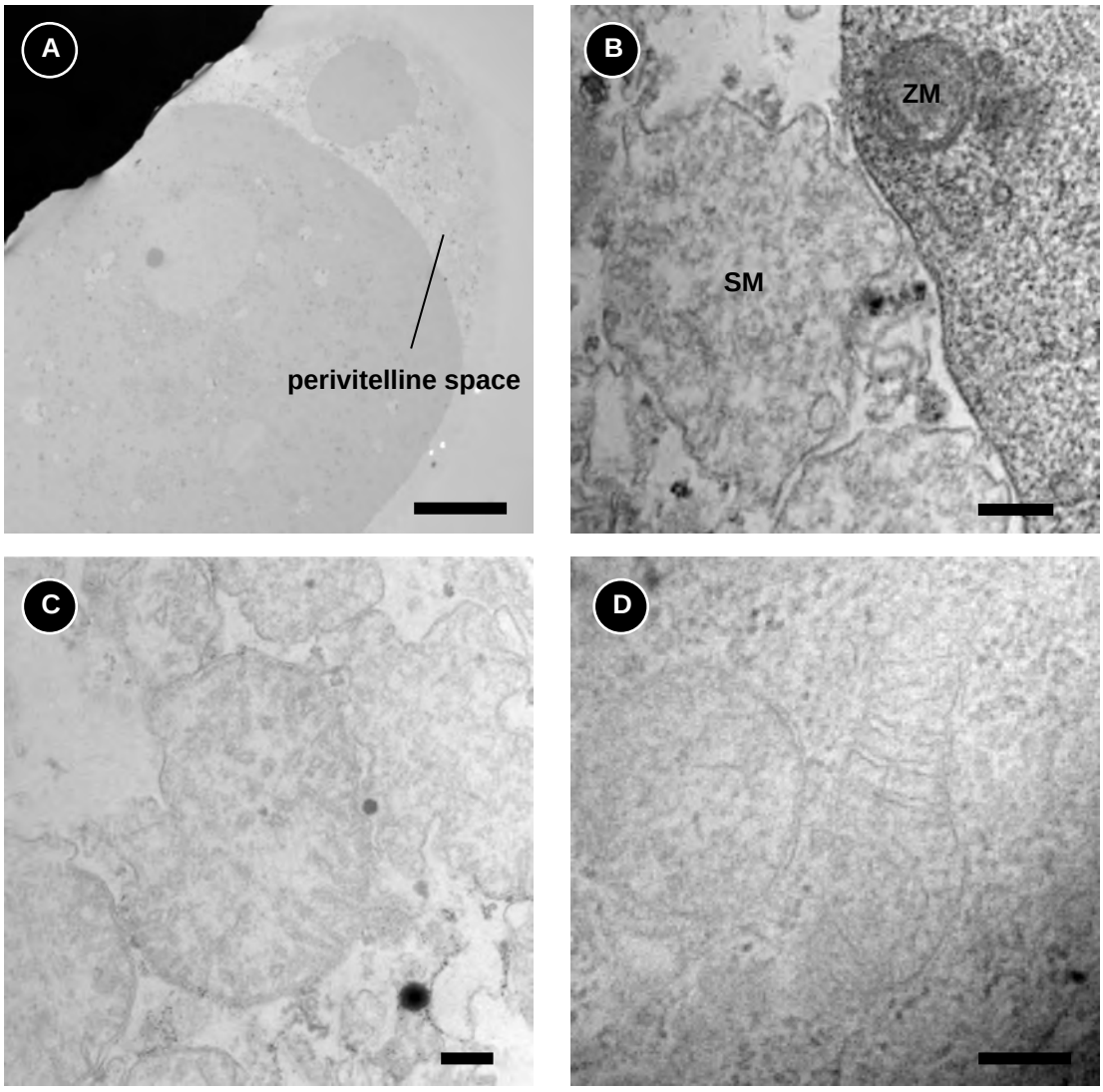


Fig.S2

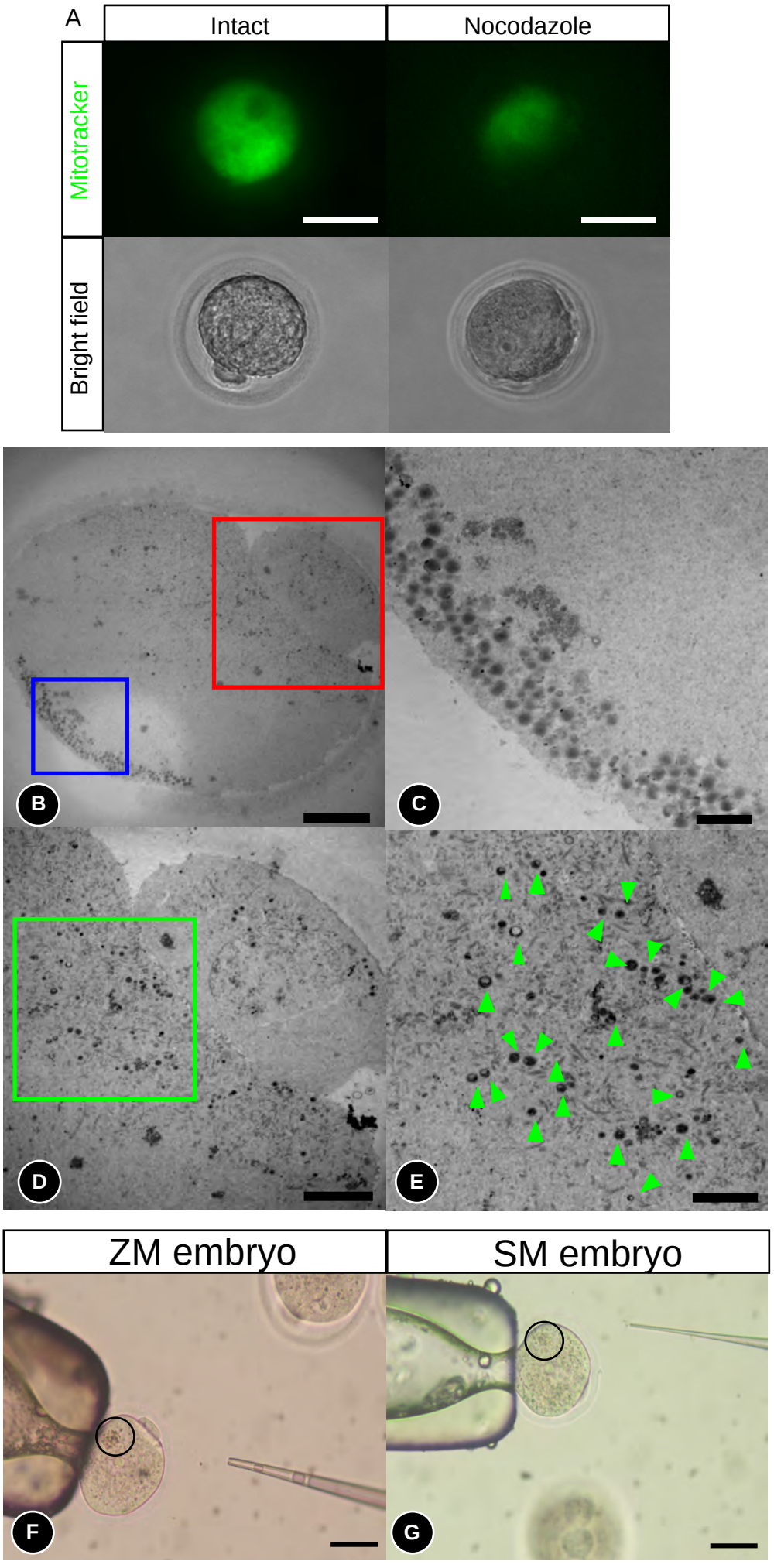

A
Intact
Nocodazole
Mitotracker
Bright field
B
C
D
E
ZM embryo
SM embryo
F
G

Fig.S3

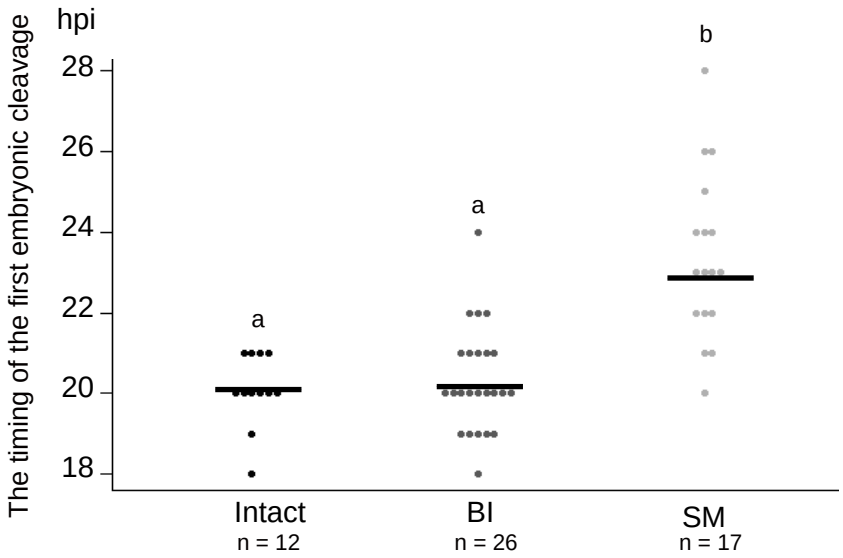
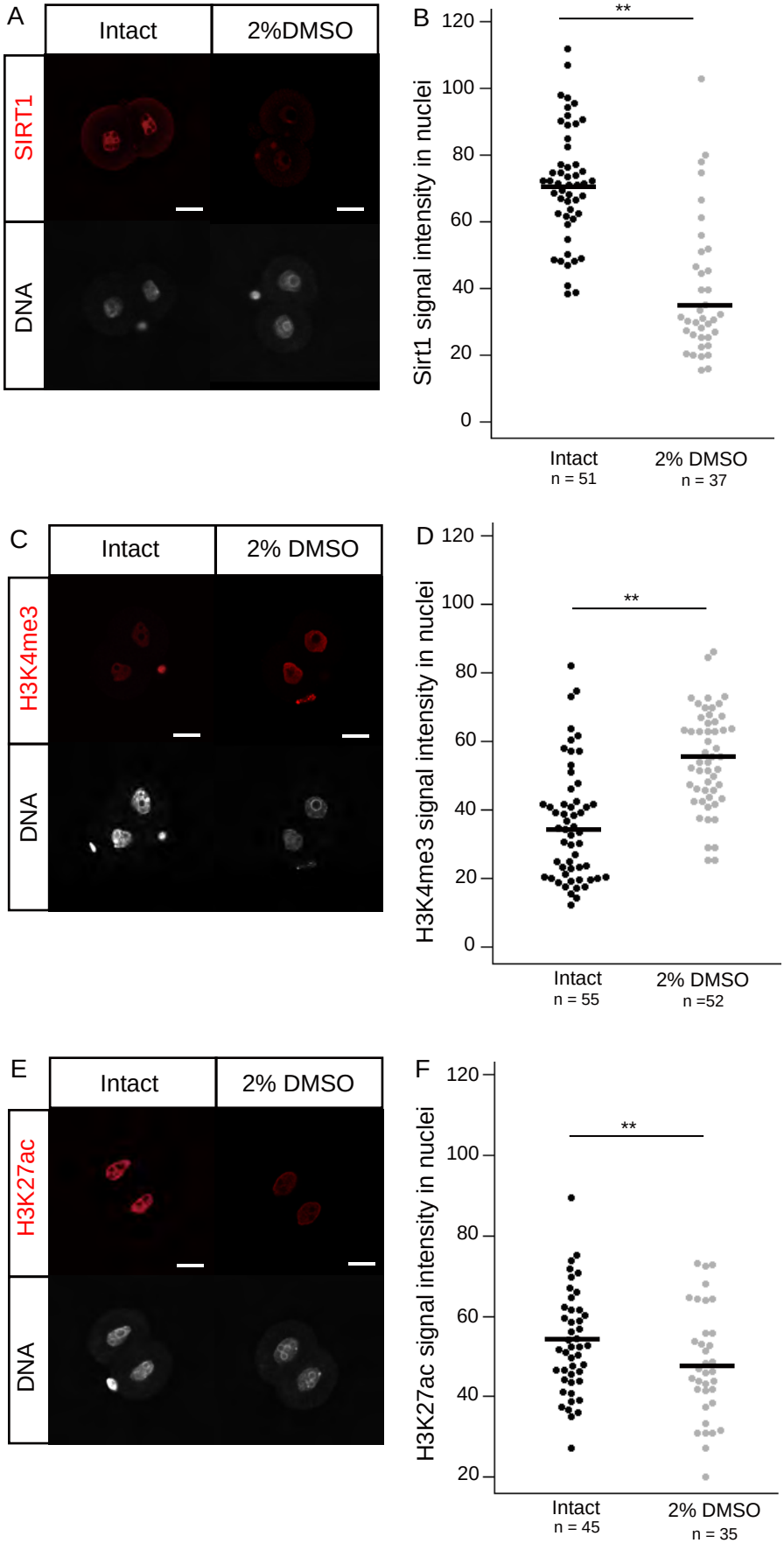

hpi
The timing of the first embryonic cleavage
28
26
24
22
20
18
a
a
b
Intact
n = 12
BI
n = 26
SM
n = 17

Fig.S4


A
Intact
2%DMSO
SIRT1
DNA
B
Sirt1 signal intensity in nuclei
120
100
80
60
40
20
0
**
Intact
n = 51
2% DMSO
n = 37
C
Intact
2% DMSO
H3K4me3
DNA
D
H3K4me3 signal intensity in nuclei
120
100
80
60
40
20
0
**
Intact
n = 55
2% DMSO
n =52
E
Intact
2% DMSO
H3K27ac
DNA
F
H3K27ac signal intensity in nuclei
120
100
80
60
40
20
**
Intact
n = 45
2% DMSO
n = 35